PERGAMON

International Journal of Heat and Mass Transfer 45 (2002) 555–570

International Journal of HEAT and MASS TRANSFER

www.elsevier.com/locate/ijhmt

Enhancement of mass transfer in a two-layer Taylor–Couette apparatus with axial flow

A.L. Yarin *, A.Yu. Gelfgat, P.Z. Bar-Yoseph

Faculty of Mechanical Engineering, Technion – Israel Institute of Technology, Haifa 32000, Israel

Received 20 March 2000; received in revised form 30 April 2001

Abstract

The effect of axial flow on the mass transfer through a liquid–liquid interface in a two-layer Taylor–Couette system is studied. The mass transfer of a passive scalar is driven by the diffusion through the boundary, enhanced by the convective mass transport due to the Taylor–Couette vortical flow, which is in turn affected by the axial pressure gradient. Numerical modeling shows that the axial flow obviates the symmetry of the distribution of the local Sherwood number, *Sh*, in a vortical cell and leads to decrease of its average counterpart. For better physical insight into this effect, simplified kinematic models of the phenomenon were considered. The numerical model shows at $Sc = 1$ to 10 (*Sc* being the Schmidt number) that the mass transfer is enhanced by vortical flow in the regions where the motion is directed towards the interface. The axial throughflow makes for elongation of the Taylor vortices in the axial direction and reduces the area of the above regions, thereby increasing the local concentration gradient and reducing the mass transfer rate. Simplified analytical results for $Sc \gg 1$ indicate redistribution of the mass flux over the interface compared with the case of $Sc = 1$ to 10. The origin of this phenomenon is explained. It is also demonstrated that *Sh* scales as $Pe^{1/2}$ for the whole range of *Sc*, *Pe* being the Peclet number of the vortical motion.

1. Introduction

The aim of the present work is to study the effect of axial flow in a two-layer Taylor–Couette apparatus on the mass transfer rate. The situation considered is relevant in the context of a novel vortex extractor for such passive scalars as, proteins. The diffusion coefficient of such admixtures is so small that purely diffusional mass transfer through liquid–liquid interfaces is too low, and it is natural to try to enhance it by means of the gradient expulsion mechanism of steady two-dimensional vortices. Two-liquid Taylor–Couette flow is considered as one of the possible flow patterns capable of creating secondary vortices for this purpose. The desired effect can also be achieved by means of secondary Dean vortices in two-fluid flows in curved or helical pipes, natural convection in a horizontal annular pipe with two-fluid throughflow, and secondary dc streaming vortical flows generated by standing or propagating waves at liquid–liquid interfaces.

The present work treats the mass transfer of a passive scalar through the liquid–liquid interface separating two immiscible cylindrical liquid layers. The fluid dynamics of such a system [1,2], as well as the enhancement of the mass transfer by a system of spatially periodic vortices [3], were recently studied for the unperturbed case without axial flow. However, as was shown for a single-layer case, axial flow strongly affects the Taylor–Couette vortex system, which necessarily leads to changes in the mass transfer rate [4]. A similar problem for the two-layer system is considered here.

The case in question falls under a wider class of problems of flow-augmented tracer/scalar dispersion. Both active (vorticity) [5] and passive (molecular admixtures or tiny particles) [6–13] scalars were considered under different flow conditions. The conclusions drawn in these works sound promising for applications in novel vortex extractors, since they indicate convection-enhanced diffusion mechanisms, which are also the aim of

* Corresponding author. Tel.: +972-4-8293-473; fax: +972-4-8324-533.

E-mail address: meralya@yarin.technion.ac.il (A.L. Yarin).

0017-9310/02/$ - see front matter
PII: S0017-9310(01)00169-7

Nomenclature

a	vortex half-length (m)
c	mass concentration
C_1, C_2, C_3	dimensionless constants in Eqs. (41), (42) and (47), respectively
d	gap between the cylinders, $R_2 - R_1$ (m)
D	diffusion coefficient ($m^2\ s^{-1}$)
$D_{21} = D_2/D_1$	dimensionless diffusion coefficient
F	dimensionless function in (21)
G	axial pressure gradient ($N\ m^{-3}$)
h	mass transfer coefficient ($m\ s^{-1}$)
p	pressure ($N\ m^{-2}$), or dimensionless
$Pe = \Omega_1 R_1 d/D_1$	Peclet number
$Pe_\infty = V_\infty a/D_1$	Peclet number in the kinematic model
r	radial coordinate (m)
R_1	radius of inner cylinder (m)
R_2	radius of outer cylinder (m)
R_i	radius of unperturbed liquid–liquid interface (m)
R_γ	radius of curvature of waviness at the interface related to the secondary vortical motion (m)
Re	Reynolds number, $\Omega_1 R_1 d/\nu_1$
Sc	Schmidt number, ν_1/D_1
Sh	local Sherwood number
$\overline{Sh}$	average Sherwood number
$Sh_N, \overline{Sh}_N$	normalized local and average Sherwood numbers
t	time (s), or dimensionless
t_d	diffusion time (s)
u	radial velocity ($m\ s^{-1}$), or dimensionless
U	dimensionless constant in Eq. (39)
$\mathbf{v}$	flow velocity ($m\ s^{-1}$), or dimensionless
v	azimuthal velocity ($m\ s^{-1}$), or dimensionless
v_{vor}	characteristic velocity of the secondary vortices ($m\ s^{-1}$)
V_∞	axial flow velocity ($m\ s^{-1}$)
w	axial velocity ($m\ s^{-1}$), or dimensionless
w_{int}	dimensional interfacial velocity ($m\ s^{-1}$)
W_{drift}	drift velocity of a steady-state flow pattern ($m\ s^{-1}$), or dimensionless
x, y	Cartesian coordinates of simplified models (m), or dimensionless
Y	position of vortex boundary (m), or dimensionless
z	axial coordinate (m), or dimensionless

Greeksymbols

γ	surface tension ($kg\ s^{-2}$)
η	dynamic viscosity ($kg\ m^{-1}\ s^{-1}$)
η_{21}	dynamic viscosity ratio, η_2/η_1
κ	ratio of diffusion coefficients
ν	kinematic viscosity ($m^2\ s^{-1}$)
ν_{21}	kinematic viscosity ratio, ν_2/ν_1
ξ, η	Cartesian coordinates of simplified model (m)
ρ	density ($kg\ m^{-3}$)
ρ_{21}	density ratio, ρ_2/ρ_1
ϕ	polar angle (rad)
ψ	stream function ($m^2\ s^{-1}$), or dimensionless
ω	uniform vorticity inside vortex (s^{-1}), or dimensionless
Ω_1	angular velocity of inner cylinder (s^{-1})
Ω_2	angular velocity of outer cylinder (s^{-1})
Ω_{21}	angular velocity ratio, Ω_2/Ω_1
Ω_*	vorticity (s^{-1})

Subscripts

1	properties related to inner fluid layer
2	properties related to outer fluid layer

the present work. Where particles are involved, however, caution is called for due to the fact that in many applications they do not constitute a passive scalar, a fact which affects their dispersion dramatically (e.g. cf. [14]).

In the present work the problem is solved numerically for a two-layer system using the finite volume method. The numerical modeling consists of two steps: (i) calculation of the flow field, and (ii) calculation of the concentration field and the mass transfer rate on the basis of the flow pattern established at step (i). The calculations show that axial flow (which is unavoidable in the novel extractor mentioned above) makes for reduction of the local and average Sherwood numbers.

The mass transfer was studied for: (1) Taylor–Couette vortical flow without axial throughflow, (2) ditto with axial throughflow, and (3) flows represented by simplified analytical kinematic models, treating pairs of vortices separated by the liquid–liquid interface.

The numerical and model results show that the mass transfer through the interface (i.e., the local Sherwood number) is increased by the vortical flow. This agrees with the gradient expulsion mechanism of steady 2D

vortices. The axial throughflow imposed on the Taylor–Couette vortical system causes axial elongation of the vortices and reduces the overall mass transfer through the interface. It is also shown that the distribution of the mass flux over the interface in the case $Sc = 1$ to 10 differs qualitatively from that for $Sc \gg 1$.

Section 2 contains the formulation of the problem and explanation of the numerical technique employed. The results of the numerical calculations are presented in Section 3. In Section 4 several simplified kinematic models are considered. Their predictions are compared with those of the numerical calculations, with a view to estimating the ability of the simplified models to predict the interfacial mass transfer rate.

2. Formulation of the problem and numerical technique

We deal with the problem of fluid flow and mass transfer through a non-deformable liquid–liquid interface in a two-layer Taylor–Couette system with axial throughflow. The system is shown schematically in Fig. 1. The inner and outer layers are attached to the corresponding cylinders which can rotate independently with angular velocities Ω_1 and Ω_2, respectively. It is assumed that the mass transfer does not affect the flow. The overall flow geometry reproduces that of the experiments in [1]. Denoting all variables and constants related to the inner and outer layers by subscripts 1 and 2, respectively, the flow in each layer is described by the Navier–Stokes and continuity equations

$$\frac{\partial \mathbf{v}_1}{\partial t} + (\mathbf{v}_1 \cdot \nabla)\mathbf{v}_1 = -\nabla(p_1 + G_1 z) + \frac{1}{Re}\Delta \mathbf{v}_1, \tag{1}$$

$$\nabla \cdot \mathbf{v}_1 = 0, \tag{2}$$

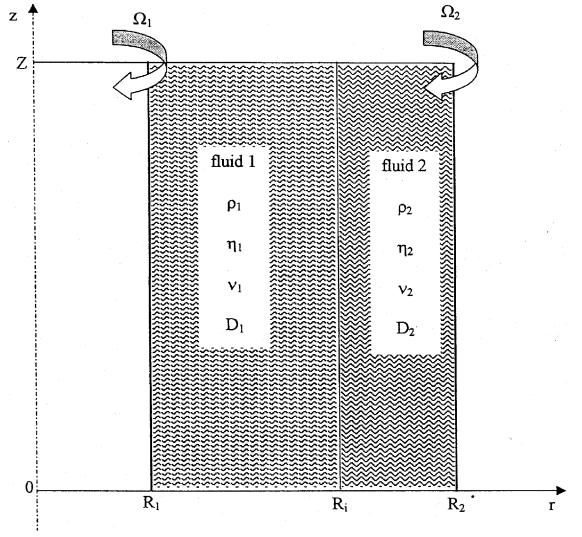

Fig. 1. Sketch of the two-layer Taylor–Couette system.

$$\frac{\partial \mathbf{v}_2}{\partial t} + (\mathbf{v}_2 \cdot \nabla)\mathbf{v}_2 = -\frac{1}{\rho_{21}}\nabla(p_2 + G_2 z) + \frac{\nu_{21}}{Re}\Delta \mathbf{v}_2, \tag{3}$$

$$\nabla \cdot \mathbf{v}_2 = 0, \tag{4}$$

where $\mathbf{v}_k = (u_k, v_k, w_k)$ is the flow velocity and $(p_k + G_k z)$ is the pressure $(k = 1, 2)$, G_1 and G_2 are the dimensionless externally imposed axial pressure gradients which create the axial flow in each of the layers independently. Furthermore, $\rho_{21} = \rho_2/\rho_1$ and $\nu_{21} = \nu_2/\nu_1$ are the density and kinematic viscosity ratios, $Re = \Omega_1 R_1 d/\nu_1$ is the Reynolds number. The length, time, velocity and pressure in (1)–(4) are rendered dimensionless by $d = R_2 - R_1$, $d/R_1\Omega_1$, $\Omega_1 R_{\text{in}}$, and $(\Omega_1 R_1)^2\rho_1$, respectively.

The problem is considered in the domain $R_1/d \leqslant r \leqslant R_2/d$, $0 \leqslant z \leqslant Z/d$ with no-slip boundary conditions at $r = R_1/d$ and $r = R_2/d$:

$$r = R_1/d: \quad u_1 = w_1 = 0, \qquad v_1 = 1, \tag{5}$$

$$r = R_2/d: \quad u_2 = w_2 = 0, \qquad v_2 = \Omega_{21} R_{21} \tag{6}$$

and periodicity conditions at $z = 0$ and $z = Z/d$:

$$\mathbf{v}_k(z = 0) = \mathbf{v}_k(z = Z/d),$$
$$p_k(z = 0) = p_k(z = Z/d), \qquad k = 1, 2, \tag{7}$$

where $\Omega_{21} = \Omega_2/\Omega_1$, and $R_{21} = R_2/R_1$. At the interface $r = R_i/d$ the usual conditions of impermeability, continuity of velocities, and balance of tangential stresses are required

$$r = R_i/d: \quad u_1 = u_2 = 0, \qquad v_1 = v_2,$$
$$w_1 = w_2, \qquad \frac{\partial v_1}{\partial r} = \eta_{21}\frac{\partial v_2}{\partial r}, \qquad \frac{\partial w_1}{\partial r} = \eta_{21}\frac{\partial w_2}{\partial r}, \tag{8}$$

where $\eta_{21} = \eta_2/\eta_1$ is the dynamic viscosity ratio.

The flow is assumed to be stably centrifugally stratified, and the interface to be non-deformable, the latter being typically the case in the experiments in question [2]. This is also supported by the following estimate. Pressure variation due to a vortex is of order ρv_{vor}^2, where v_{vor} is the characteristic velocity of the secondary vortex motion. It should be compensated by the restoring force – surface tension. Denoting the surface tension coefficient by γ, the radius of curvature of the interfacial waviness corresponding to the vortices is of order $R_\gamma = \gamma/\rho v_{\text{vor}}^2$. Taking the characteristic values of $\gamma = 50 \times 10^{-3}$ kg/s^2, $\rho = 10^3$ kg/m^3 and $v_{\text{vor}} = 0.6 \times 10^{-2}$ m/s, we obtain $R_\gamma = 1.39$ m, which is much larger than either R_1 or R_2 – both of which are of order 0.1 m. Thus the waviness is negligibly small compared to the mean curvature of the interface.

With the steady-state flow calculated, the mass transfer problem is considered. Here we assume that the time needed to reach steady state is much shorter than the characteristic diffusion time, so that the mass transfer during the transient stage is negligibly small. Besides, the effect of the axial throughflow must be taken

into account. Due to the latter the steady flow pattern can drift axially with a constant dimensionless drift velocity W_{drift} [4,9]. Then the mass transfer should be studied in a frame of reference associated with moving vortices (which are steady in this frame). The mass transfer equations in the two fluid layers are

$$\frac{\partial c_1}{\partial t} + (\mathbf{v}_1 \cdot \nabla)c_1 - W_{\text{drift}}\frac{\partial c_1}{\partial z} = \frac{1}{Pe}\Delta c_1, \tag{9}$$

$$\frac{\partial c_2}{\partial t} + (\mathbf{v}_2 \cdot \nabla)c_2 - W_{\text{drift}}\frac{\partial c_2}{\partial z} = \frac{D_{21}}{Pe}\Delta c_2, \tag{10}$$

where c_k, $k = 1, 2$, are the concentrations of a passive scalar in the fluid layers, $D_{21} = D_2/D_1$ is the diffusion coefficient ratio, $Sc = \nu_1/D_1$ is the Schmidt number and $Pe = ScRe$ is the diffusional Peclet number. The concentration is rescaled as $c = (c - c_{\min})/(c_{\max} - c_{\min})$, where $c_{\max}$ and $c_{\min}$ are the maximal and concentration at zero time, at which the inner fluid layer is assumed to contain a uniformly distributed admixture, which starts to diffuse into the outer layer. The boundary and initial conditions for the mass transfer problem are:

$$r = R_1/d \text{ or } R_2/d: \quad \frac{\partial c}{\partial r} = 0, \tag{11}$$

$$z = 0, Z/d: \quad \frac{\partial c}{\partial z} = 0, \tag{12}$$

$$r = R_i/d: \quad c_1 = c_2, \qquad \frac{\partial c_1}{\partial r} = D_{21}\frac{\partial c_2}{\partial r}, \tag{13}$$

$$t = 0: \quad c_1 = 1, \qquad c_2 = 0. \tag{14}$$

For characterization of the mass transfer, the local and average Sherwood numbers are defined as:

$$Sh(z) = \left.\frac{\partial c}{\partial r}\right|_{r=R_i/d}, \quad \overline{Sh} = \frac{d}{Z}\int_0^{Z/d}\left.\frac{\partial c}{\partial r}\right|_{r=R_i/d}\mathrm{d}Z. \tag{15}$$

The Sherwood number was calculated for the inner layer. Since we are interested in its change relative to the no-flow or no-vorticity states, the choice of side is arbitrary.

The problems (1)–(8) and (9)–(14) are solved numerically using the finite volume method with the solver based on the SIMPLE algorithm with semi-implicit three-level time integration scheme, used in [15,16] for swirling flows in a cylindrical container. The steady-state fluid flow can be calculated with a dimensionless time step $\tau = 0.1$ (usually, several thousands of time steps are necessary to reach a converged solution). Since the semi-implicit scheme is unsuitable for the mass transfer problem (11)–(14) (at large time intervals the time derivative vanishes, and the boundary conditions of the problem tend to the Neumann type, so that the corresponding set of linear algebraic equations becomes almost singular, which leads to spurious numerical errors) we use an explicit two-level scheme for the time integration. To ensure numerical stability at large Peclet numbers ($Pe \sim \mathrm{O}(10^4)$), the calculations are performed with a small time step $\tau = 10^{-3}$. The reported flow and mass transfer calculations are done on the same staggered grid, compressed near the interface. The interface passes through the center of the radial velocity cell, and therefore through the edge of the concentration cell. This permitted direct implementation of the non-penetration condition. The concentration was considered as a function distributed over the whole domain, whereby the concentration continuity condition was implemented. The jump in the mass transfer coefficient (as well as those in the density and viscosity) was smoothed over 6 mesh layers, using the smoothed Heaviside function defined as the integral of Peskin's kernel [17]. Then the mass transfer equation (as well as the Navier–Stokes equation) was considered as defined over the whole domain. Our numerical experiments showed no significant changes in the results (up to the third decimal digit) when we used 4, 6, 8 or 10 mesh layers for the smoothing.

To ensure mesh- and time-step independence of the results, the calculations for the largest value of the Peclet number $Pe = 10^4$ were repeated on 100×100 and 200×200 grids with time steps $\tau = 10^{-3}$ and 10^{-4}. No changes were found. Most of the results reported below refer to the 100×100 grid and $\tau = 10^{-3}$. The calculations always started from the Couette flow, since numerical initialization of the Taylor instability (e.g. by allowing the round-off errors to grow) takes a very long time. An initial perturbation, which allows for triggering the onset of Taylor vortices, was proposed in [18]. We extended it to the two-layer case.

Following [6] we define the turnover, diffusion and averaging time as $T_{\text{e}} = d/\Omega R_1$, $T_{\text{d}} = d^2/D_1$ and $T_{\text{a}} = T_{\text{d}}Pe^{-2/3}$, respectively. Using the time scale $d/\Omega R_1$, we obtain the following dimensionless values: $T_{\text{e}} = 1$, $T_{\text{d}} = Pe$, and $T_{\text{a}} = Pe^{1/3}$. In the calculations described below the dimensionless time of integration was 300 or 400, so that for $Pe = 1000$–$10,000$ the integration time was always shorter than the diffusion time and longer than the averaging time.

3. Results of calculations

Our calculations retained the set of parameters reported in [1,2]: $R_1/R_2 = 0.827$, $Z/d = 1$, $\eta_{21} = 0.96$, $\rho_{21} = 1.4$, $\Omega_{21} = 0.62$, $Re = 4490$. Regarding the effect of the axial throughflow, we consider two cases: (i) without axial flow $G_1 = G_2 = 0$, and (ii) with axial flow $G_1 = G_2 = 0.0005$ and (iii) ditto, $G_1 = G_2 = 0.001$. Streamlines of the calculated flows are shown in Fig. 2.

According to the linear stability results of [2] and the experiments [1,2] the Taylor vortices in the two-layer system have an almost square cross-section. Accordingly, we chose the aspect ratio as 1:1, which accommodates two pairs of the Taylor vortices (Fig. 2(a)).

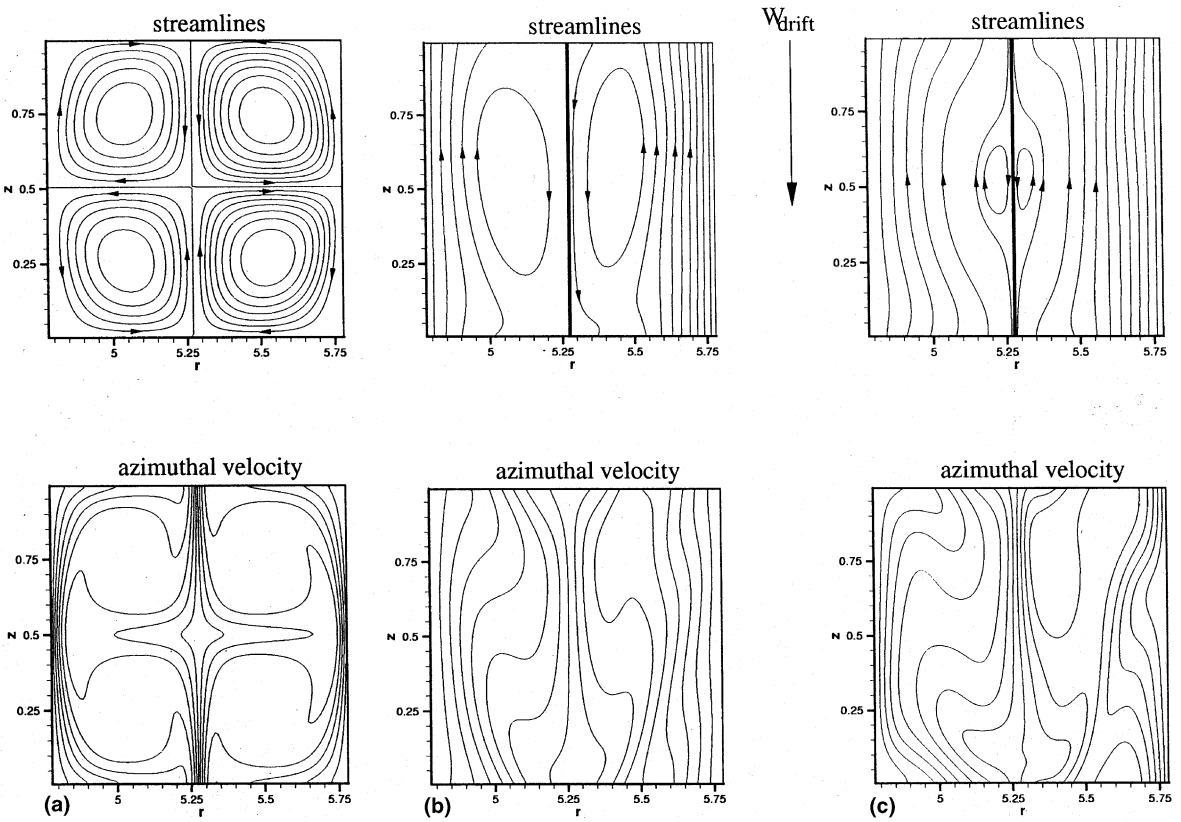

Fig. 2. Streamlines and isolines of the azimuthal velocity of the two-layer Taylor–Couette flow $Re = 4490$: (a) $G_1 = G_2 = 0$; fixed frame. (b) $G_1 = G_2 = 0.0005$; moving frame. (c) $G_1 = G_2 = 0.001$; moving frame.

Periodic boundary conditions were implemented between the cells, whereby long gaps similar to those in the experiments were actually modeled.

Without an axial pressure gradient ($G_1 = G_2 = 0$), the flow pattern consists of a pair of counter-rotating antisymmetric Taylor vortices in each layer (Fig. 2(a)). This pattern is disrupted by the axial flow, initiated by instantaneous switch-on of the axial pressure gradient. As noted above, the steady flow pattern moves axially with a constant drift velocity, in this case found to be $W_{\text{drift}} = -0.0495$ and -0.0513 for $G_1 = G_2 = 0.0005$ and 0.001, respectively. The stream function and isolines of the azimuthal velocity calculated in the frame moving axially with the drift velocity, are shown in Fig. 2(b) and (c). In the case represented by Fig. 2(b), with $|W_{\text{drift}}| = 0.0495$, the maximal radial velocity is 0.00984. The maximal axial velocity (which comprises the basic axial flow and the secondary meridional flow) is 0.0730. Therefore, compared to the radial velocity, the drift velocity is about five times larger than the maximal velocity in the vortex. Under the impact of the axial throughflow, the Taylor vortices become elongated in the axial direction and retain the opposite direction of rotation, namely, the flow is directed towards the interface in the upper part of the vortex and away from it in the lower part. The axial throughflow is directed downwards and has a Poiseuille-like profile, so that the axial velocity is maximal near the interface and tends parabolically to zero near the boundaries in a fixed frame. Therefore, in a frame moving downwards at the drift velocity, a vortex pair experiences a downward flow near the interface, and an upward flow near the boundaries (Fig. 2(b) and (c)). As the axial pressure gradient increases the vortices become smaller, as in the single-layer case [4].

Calculations of the mass transfer were carried out for a fixed Reynolds number $Re = 4490$, three fixed Peclet numbers $Pe = 10^3$, 5×10^3 and 10^4, and three fixed diffusion coefficient ratios $D_{21} = 0.5$, 1 and 2. Snapshots of the concentration distribution at several fixed moments of time are shown in Figs. 3 and 4. These figures illustrate how the concentrations in both layers equalize in time. It is also seen that in the inner layer (where the passive scalar is initially located) the higher concentrations fall in the regions where the flow velocity is directed towards the interface (cf. Fig. 2(a) and (b) vs. Figs. 3 and 4, respectively) and the local concentration gradient near the interface is larger. This leads to intensification of the

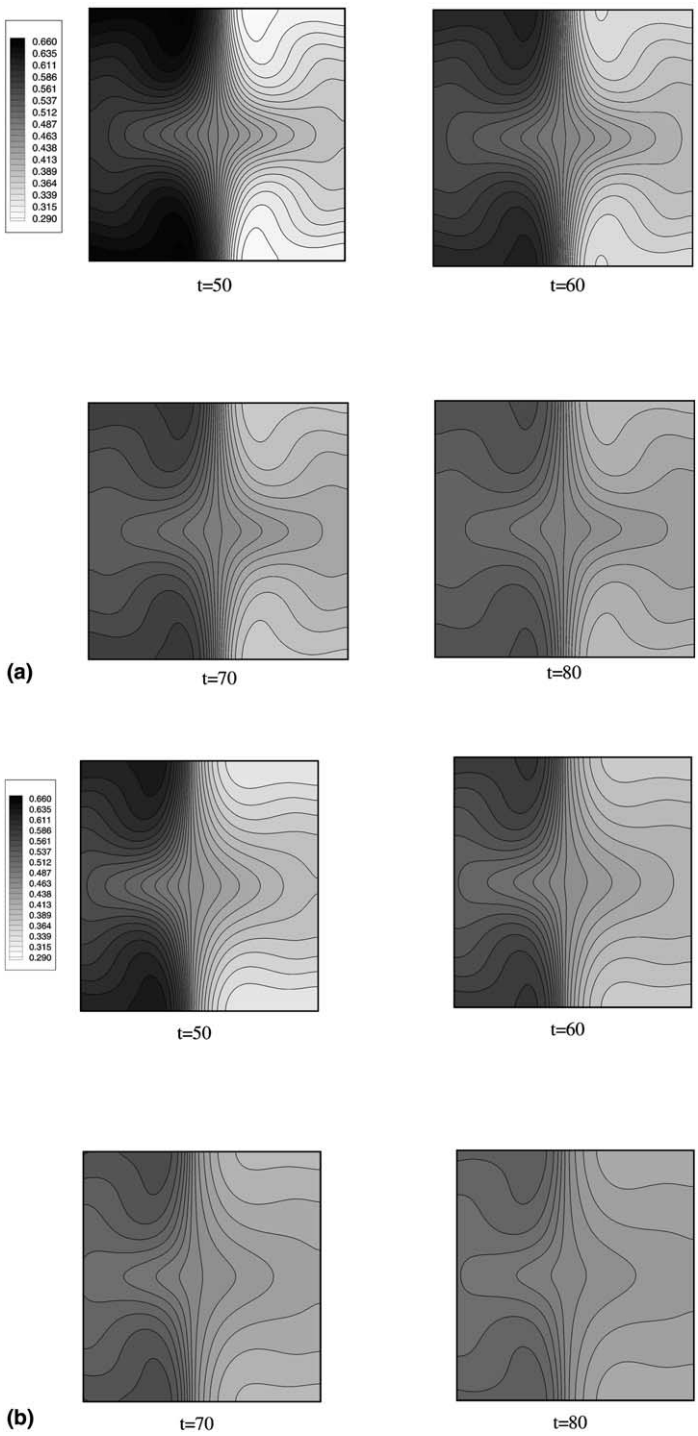

Fig. 3. Concentration contours without throughflow. $Re = 4490$, $Pe = 1000$, $G = 0$: (a) $D_{21} = 1$; (b) $D_{21} = 2$.

interfacial mass transfer in these regions. This latter effect will be discussed below in detail.

The time histories of the total volume fraction of the passive scalar that passed from the inner to the outer layer are shown in part (a) of Figs. 5–7, and their counterparts for the average Sherwood number $\overline{Sh}$ (15) in part (b) of Figs. 5–7. Note that since the Reynolds number is fixed throughout, increase of the Peclet

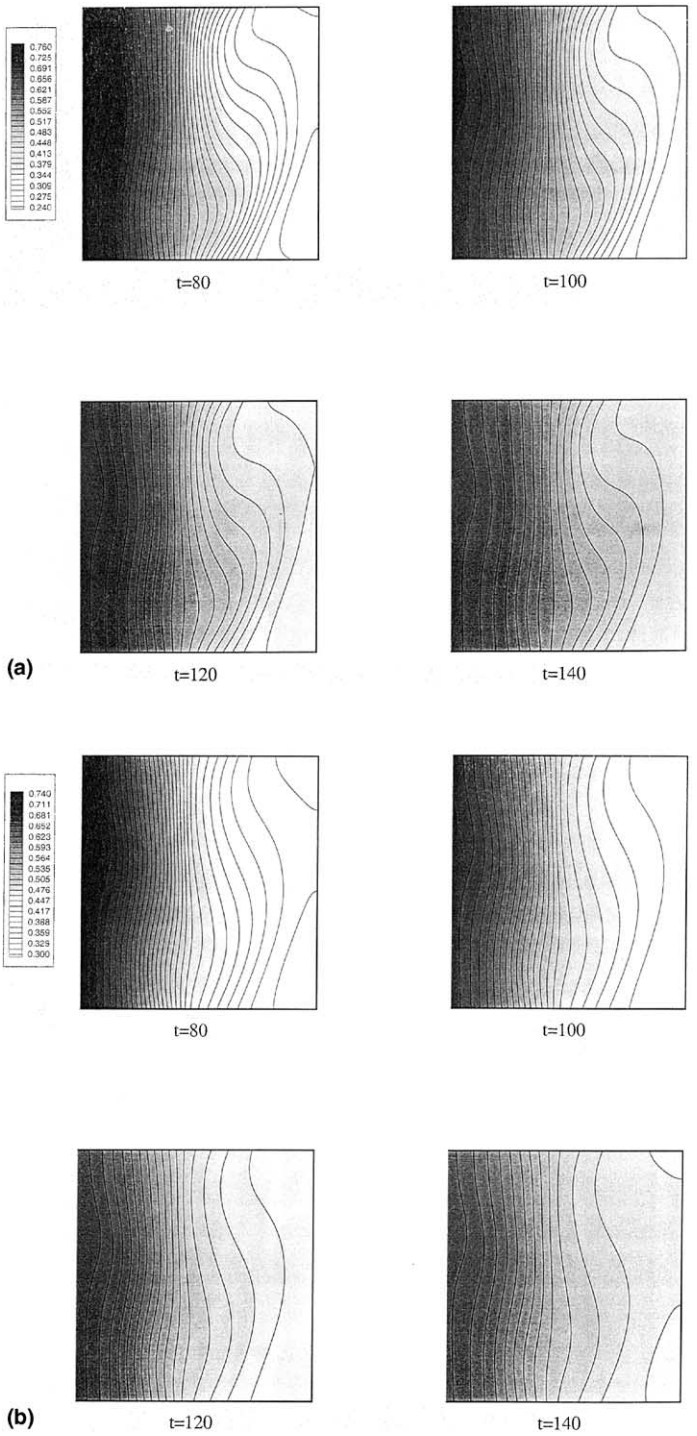

Fig. 4. Concentration contours with throughflow. $Re = 4490$, $Pe = 1000$, $G = 0.0005$: (a) $D_{21} = 1$; (b) $D_{21} = 2$.

number means decrease of the diffusion coefficient D_1 in the inner layer. For a fixed Peclet number, in all the cases considered increase of the diffusion coefficient ratio $D_{21} = D_1/D_2$ manifests itself as slightly faster growth of the volume fraction. In other words, a larger diffusion coefficient in the initially "empty" layer makes for more intensive mass transfer. It is obvious that the average Sherwood number tends to zero as time tends to infinity,

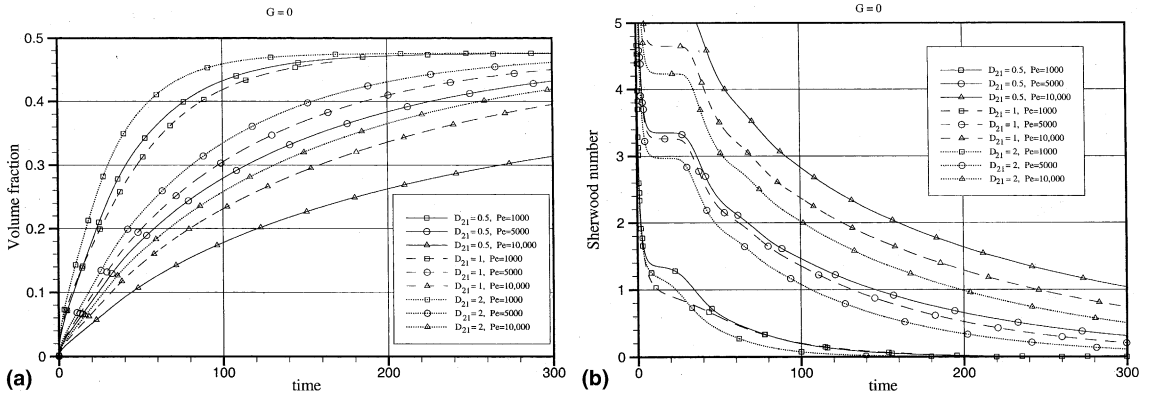

Fig. 5. (a) Volume fraction vs. time without throughflow. (b) Average Sherwood number vs. time without throughflow.

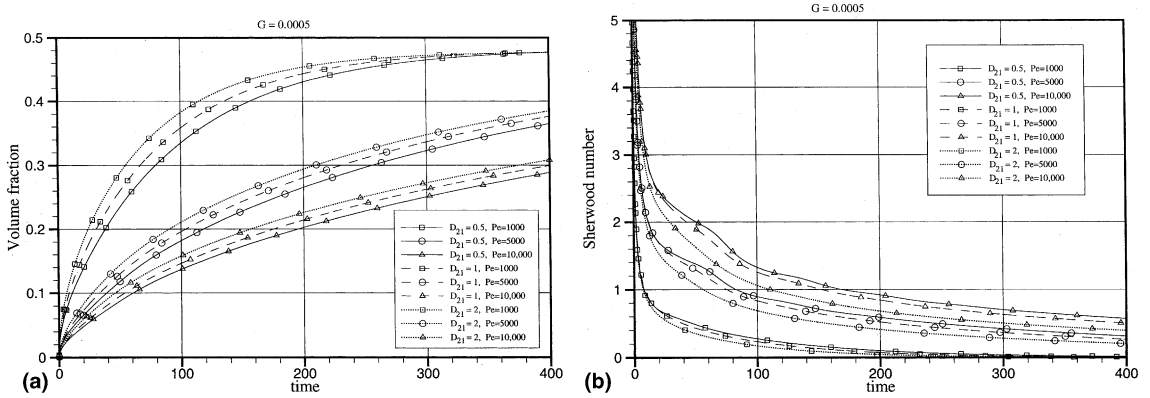

Fig. 6. (a) Volume fraction vs. time for throughflow corresponding to $G = 0.0005$. (b) Average Sherwood number vs. time for throughflow corresponding to $G = 0.0005$.

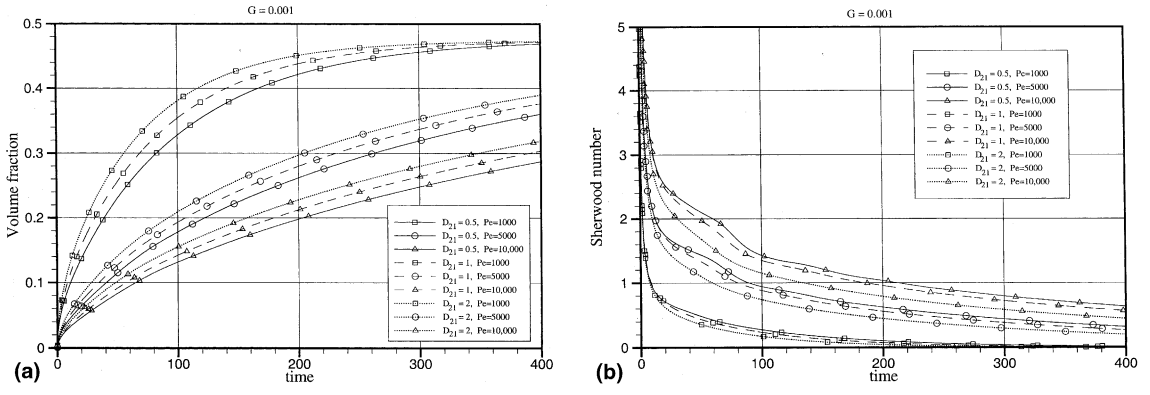

Fig. 7. (a) Volume fraction vs. time for throughflow corresponding to $G = 0.001$. (b) Average Sherwood number vs. time for throughflow corresponding to $G = 0.001$.

and the concentrations in the two layers equalize. This tendency is clearly seen in part (b) of Figs. 5–7. Comparison of part (a) of Figs. 5–7 with part (b) of Figs. 5–7 shows that the average Sherwood number is larger when the volume fracture is smaller. This is quite apparent, since a smaller volume fraction means less mixing and therefore larger concentration gradients near the interface, which in turn, make for larger average Sherwood numbers. Note that according to [7] the average Sherwood number increases as $Pe^{1/2}$ with $Pe \to \infty$. This

trend is clearly seen in part (b) of Figs. 5–7. The scaling relating $\overline{Sh}$ with Pe will be dealt with below.

Further information about the axial flow effect on the mass transfer can be drawn from the profiles of the local Sherwood numbers. For further comparison with the analytical results (see Section 4), we introduce the characteristic values $c_\infty^{(1)}$ and $c_\infty^{(2)}$ defined as the maximal concentration values at a distance of 10 grid layers (about 9% of the gap width) from the interface in the first and second layers, respectively. Then we normalize the Sherwood number by their difference $(c_\infty^{(1)} - c_\infty^{(2)})$, such that $Sh_N(x) = Sh(x)/(c_\infty^{(1)} - c_\infty^{(2)})$ and $\overline{Sh}_N = \overline{Sh}/(c_\infty^{(1)} - c_\infty^{(2)})$. Both $\overline{Sh}_N$ and $Sh_N(x)$ tend to a constant (value and function) as time tends to infinity (Figs. 8 and 9(a)–(c)). The latter three figures refer to cases (i) $G = 0$, (ii) $G = 0.0005$ and (iii) $G = 0.001$, respectively. In case (i), without axial flow (Fig. 8(a)), the profile of $Sh_N(z)$ is symmetric with respect to $z = 0.5$, and the local Sherwood number is maximal at the points where the radial velocity is directed towards the liquid–liquid interface and minimal in the opposite situation. In cases (ii) and (iii) the profile of $Sh(z)$ is asymmetric due to the asymmetry of the flow, but otherwise its behavior is the same as in case (i). Comparing the three figures one can see that at the same values of the Peclet number the maximal values of Sh are lower in the presence of the axial flow.

The increase in the average Sherwood number with the Peclet number can be explained as follows. The mass transfer through the interface is governed by the boundary condition (13). Namely, it is determined by the diffusion coefficient ratio and by the radial component of the concentration gradient in the vicinity of the interface. For a fixed diffusion coefficient ratio the mass transfer can be increased only by increase of the radial concentration gradient near the surface. The latter is provided by the convective transport of the scalar due to the Taylor vortex flow. The effect is strongest in the area where flow in the vortices is directed towards the interface, so that the higher concentration in the inner layer and lower concentration in the outer layer are advected towards the interface (see also Figs. 3 and 4). However, as will be shown below, this is not the only factor affecting the mass transfer (cf. the end of Section 4).

Fig. 10 illustrates how the time-asymptotic values of the normalized average Sherwood number vary with $Pe^{1/2}$. For Taylor vortex flow unaffected by throughflow $(G = 0)$ the dependence $\overline{Sh}_N(Pe^{1/2})$ tends to be linear, starting from $Pe \approx 5000$. Axial throughflow suppresses the vortices (Fig. 2), and therefore larger Peclet numbers are needed to reach the linear dependence. The latter is illustrated in Fig. 10(b), where it is still not reached at $Pe = 10000$.

It is emphasized that 3D and time-dependent instabilities are not expected in the present range of parameters. Indeed, according to the results of [19] co-rotation stabilizes the flow. Our outer Reynolds number is about 2800, which is far beyond the stability diagram of [19]. Besides, the linear stability results of [2] obtained for the two-layer case show that all the transitions take place at significantly larger Reynolds numbers than in the single-layer case. Moreover, it is well known that the axial throughflow has a strong stabilizing effect. Since no azimuthal waves were observed in the experiments [1,2] used for determining our parameters, we refrain from looking for 3D and time-dependent instabilities. Where we are slightly beyond the axisymmetry-3D transition limit, a small azimuthal modulation of the flow can hardly have a significant influence on the results.

Note also that the linear stability analysis of [20] for a single-layer case showed a slow change in the critical wave number until the axial gradient exceeded a certain value. Similar behavior of the critical wave number was observed in [21] for the two-layer case, with countercurrent flow in the axial direction. To the best of our

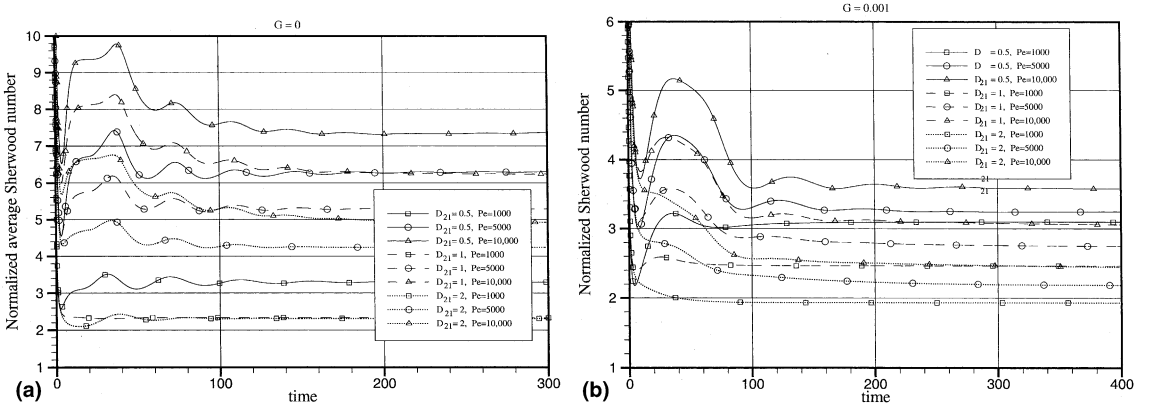

Fig. 8. Normalized average Sherwood number vs. time $Re = 4490$: (a) without throughflow $G = 0$; (b) with throughflow corresponding to $G = 0.001$.

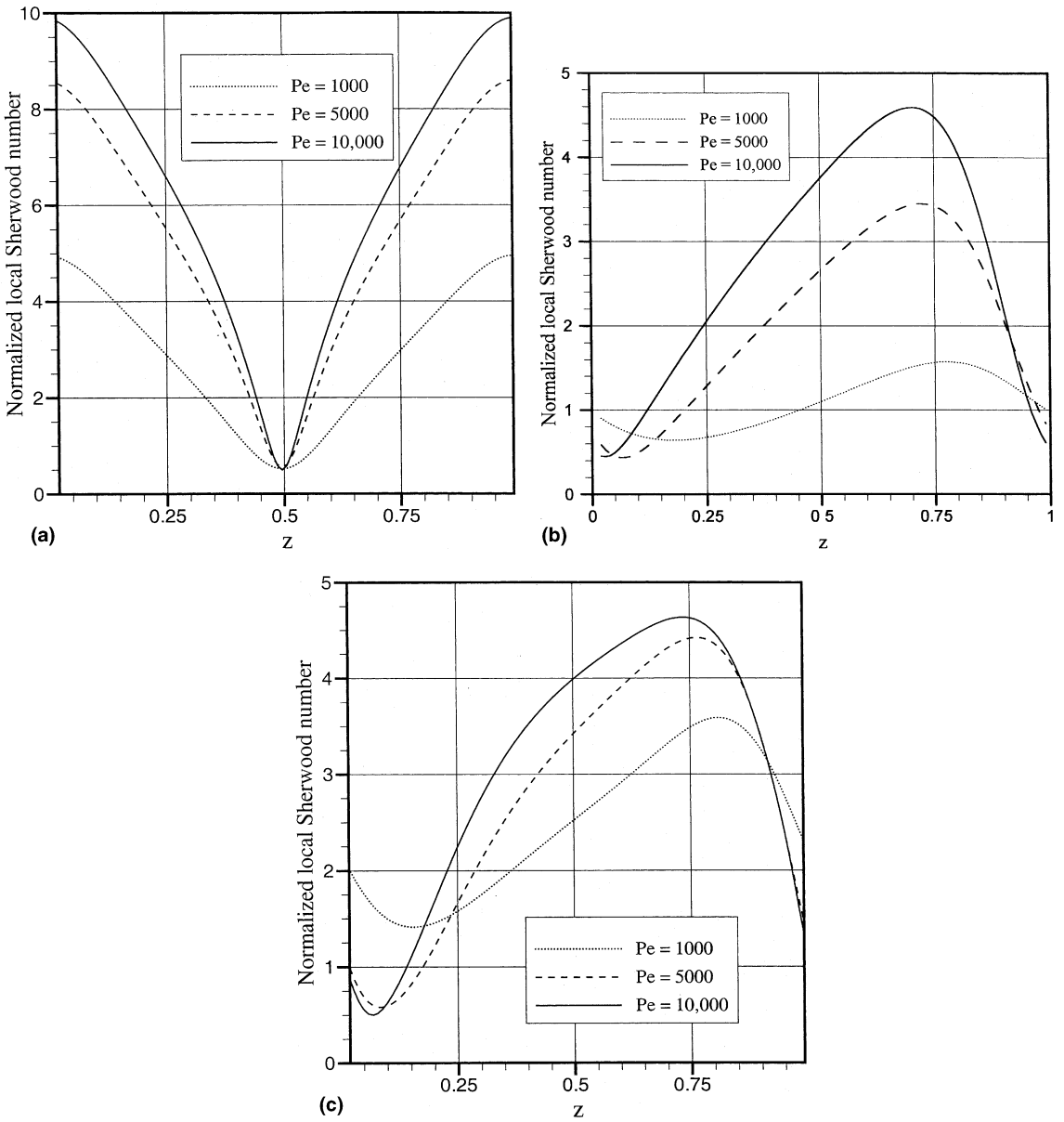

Fig. 9. Normalized local Sherwood number for $Re = 4490, D_{21} = 1$. (a) $G_1 = G_2 = 0$, (b) $G_1 = G_2 = 0.0005$, (c) $G_1 = G_2 = 0.001$.

knowledge, there is no published linear stability results for a two-layer case with axial co-flow, like the one considered in the present work. It is clear that if we set the aspect ratio of the computational domain according to the critical wave number (which is not known for the case considered), the intensity of the vortical flow will increase and so will its effects on the mass transfer. However, so long as the spatial period does not differ significantly from unity, the results will remain qualitatively the same. Also, it was shown that for large Peclet numbers the mass transfer coefficient (the Sherwood number) is scaled as $Pe^{1/2}$, which allows one to estimate the effect for similar vortical flows. One of the purposes of our study was to compare the effect of Taylor vortices affected and unaffected by the axial flow on the mass transfer. To make comparison easier, we used the same computational domain.

4. Simplified kinematic models

Numerical results (Section 3and [4]) show that with a significantly weak axial flow in a two-layer Taylor–Couette apparatus, there appear a system of vortex pairs

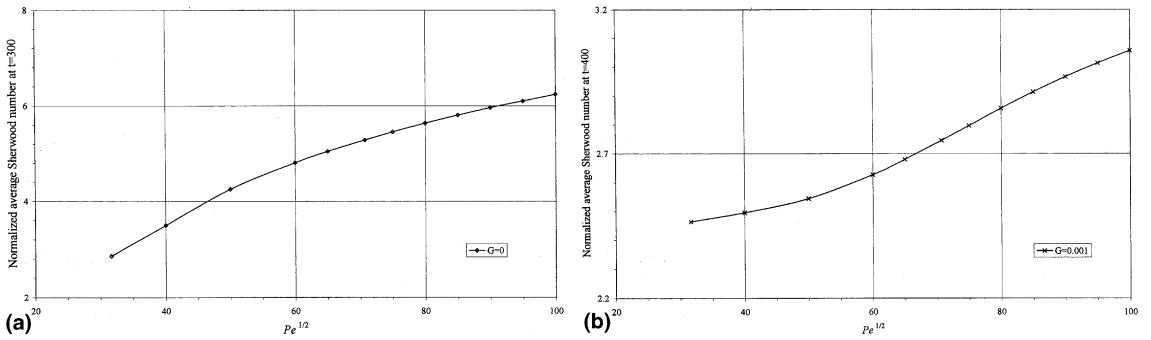

Fig. 10. Scaling of the normalized average Sherwood vs. Peclet number for $Re = 4490, D_{21} = 1$. (a) $G_1 = G_2 = 0$, (b) $G_1 = G_2 = 0.001$.

moving in the axial direction relative to the fluid flow, the vortices in the pairs remaining axisymmetric as in the case without axial flow. Enhancement of the mass transfer of a passive scalar from one fluid to another is related, first of all, to these vortices. In the present section we employ first a simple kinematic model mimicking a single pair of vortices in a parallel unbounded flow and predict its effect on the mass transfer. In the proposed kinematic model (designated 1), we disregard the effect of cylinder curvature in the apparatus, since it is expected to be insignificant for gaps much smaller than the cylinder radius. Accordingly, a planar model is considered. The flow pattern to be employed was discussed in [22]. It is sketched in Fig. 11, with the frame of reference associated with the vortices. Fluids 1 and 2 occupy the domains $y < 0$ and $y > 0$, respectively. The vortex pair is surrounded by a boundary Γ, to be determined in the course of the solution. Along the x-axis the vortices span a distance $2a$. A parallel flow impinges on the vortices with velocity V_∞. For the vortices we assume constant vorticities of magnitude $(-\omega)$ in fluid 1 and $(+\omega)$ in fluid 2, respectively, the value of ω also to be found in the course of the solution. This kinematic model belongs to the class of flows discussed in [5]. Mass transfer of a passive scalar at the interface $-a \leqslant x \leqslant a$, $y = 0$ is expected to be enhanced by the vortical

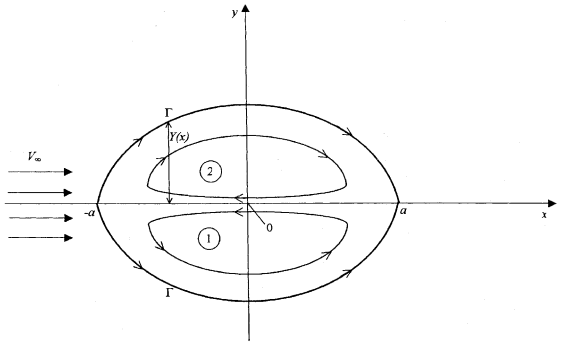

Fig. 11. Sketch of the flow pattern of kinematic model 1.

motion, which propels the admixture rapidly towards the interface, sustaining there a steep concentration gradient.

The vortical component of the flow is determined by the Poisson equation for the vortical stream function ψ_v, namely

$$\Delta\psi_v = \Omega_*, \tag{16}$$

where $\Omega_* = \pm\omega$ in the vortices as above and $\Omega_* = 0$ outside the domain S bounded by Γ.

The solution of the Poisson equation (16) is given by

$$\psi_v = \frac{1}{2\pi}\int_S\int \Omega_* \ln r \,\mathrm{d}\xi\,\mathrm{d}\eta, \tag{17}$$

where $r = [(x-\xi)^2 + (y-\eta)^2]^{1/2}$, and ξ, η are dummy Cartesian coordinates.

Eq. (17) can be supplemented by a stream function of the (potential) parallel flow $\psi_p = V_\infty y$ yielding the stream function ψ of the flow in Fig. 11

$$\psi = \psi_p + \psi_v. \tag{18}$$

Therefore, from (17) and (18) we find

$$\psi(x,y) = V_\infty y + \frac{\omega}{4\pi} \times \int_{-a}^{a} \mathrm{d}\xi \int_0^{Y(\xi)} \ln\left[\frac{(x-\xi)^2 + (y-\eta)^2}{(x-\xi)^2 + (y+\eta)^2}\right] \mathrm{d}\eta, \tag{19}$$

where $Y(\xi)$ is the y-coordinate of the boundary Γ.

To find Γ we should substitute $y = Y(x)$ and $\psi = 0$ in Eq. (19), which yields the following dimensionless equation for Y:

$$Y(x) + \frac{\omega}{4\pi}\int_{-1}^{1} \mathrm{d}\xi \int_0^{Y(\xi)} \ln\left[\frac{(x-\xi)^2 + (Y(x)-\eta)^2}{(x-\xi)^2 + (Y(x)+\eta)^2}\right] \mathrm{d}\eta = 0. \tag{20}$$

Here and hereinafter we render the parameters dimensionless using the following scales: a – for x, y, ξ, η,

and $Y; V_\infty/a$ – for ω, and V_∞ – for the velocity components.

Evaluating the inner integral in (20), we arrive at the following equation for $Y(x)$ of Γ:

$$Y(x) + \frac{\omega}{4\pi}\int_{-1}^{1} F[\xi, x, Y(x)]\,\mathrm{d}\xi = 0, \quad -1 \leqslant x \leqslant 1, \tag{21}$$

where

$$\begin{aligned} F[\xi, x, Y(x)] = {} & 2Y(x)\ln\left[(x-\xi)^2 + Y^2(x)\right] - 4Y(x) \\ & + 4(x-\xi)\ \arctan\left[\frac{Y(x)}{x-\xi}\right] \\ & - [Y(x) - Y(\xi)]\ln\left[(x-\xi)^2\right. \\ & \left. + (Y(x) - Y(\xi))^2\right] + 2[Y(x) - Y(\xi)] \\ & - 2(x-\xi)\arctan\left[\frac{Y(x) - Y(\xi)}{x-\xi}\right] \\ & - [Y(x) + Y(\xi)]\ln\left[(x-\xi)^2\right. \\ & \left. + (Y(x) + Y(\xi))^2\right] + 2[Y(x) + Y(\xi)] \\ & - 2(x-\xi))\ \arctan\left[\frac{Y(x) + Y(\xi)}{x-\xi}\right]. \end{aligned} \tag{22}$$

The velocity components are readily found by differentiating (19). In particular, the interfacial velocity is given by

$$w_{\mathrm{int}}(x) = 1 - \frac{\omega}{2\pi}\int_{-1}^{1} \ln\left[\frac{(x-\xi)^2 + Y^2(\xi)}{(x-\xi)^2}\right]\mathrm{d}\xi. \tag{23}$$

At the bifurcation points $x = \pm a$, $y = 0$ the velocity should be zero, which yields the following dimensionless equation for ω:

$$\omega = \frac{2\pi}{\int_{-1}^{1} \ln\left\{1 + [Y(\xi)/(\xi+1)]^2\right\}\mathrm{d}\xi}. \tag{24}$$

Note that $[Y(\xi)/(\xi+1)^2]|_{\xi\to -1}$ tends to $[\mathrm{d}Y/\mathrm{d}\xi]^2|_{\xi=-1}$.

Solving Eqs. (21) and (24), we find the vorticity ω and the shape of the boundary Γ, $Y(x)$. The vorticity equals

$$\omega = 6.457 \tag{25}$$

and the calculated shape of the boundary $\Gamma, Y(x)$, is shown in Fig. 12.

Knowing $Y(x)$ and ω, we calculate the interfacial velocity $w_{\mathrm{int}}(x)$ from (23). The result is shown in Fig. 13, where it is seen that to the left of the vortex tip (at $x < -1$) $w_{\mathrm{int}} > 0$, inside the vortex pair (at $|x| \leqslant 1$) $w_{\mathrm{int}} < 0$), and to the right of the vortex pair (at $x > 1$) the interfacial velocity becomes positive once more, as it should be for the flow as per Fig. 11.

The flow field as a whole is found from (19), rendered dimensionless. The results are shown in Fig. 14.

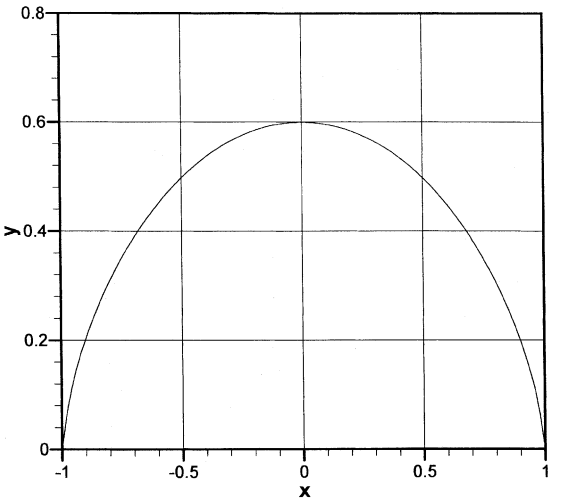

Fig. 12. The shape of the vortex boundary (kinematic model 1).

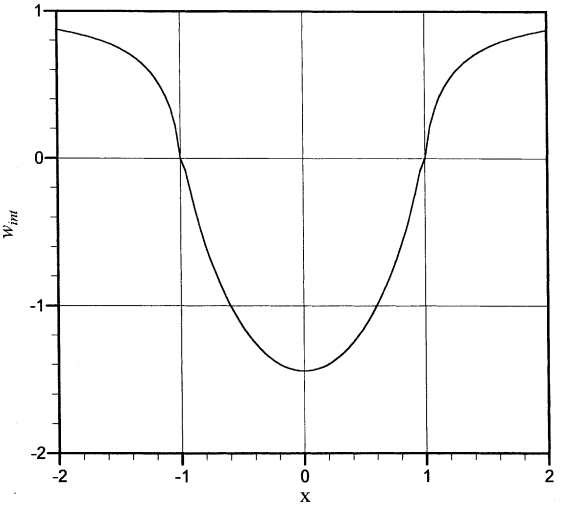

Fig. 13. The interfacial velocity distribution (kinematic model 1).

Consider now the mass transfer of a passive scalar through the interface. We assume that the Schmidt number on both sides is much larger than unity, $Sc \gg 1$ ($Sc_i = \nu_i/D_i$), and very thin diffusional boundary layers appear near the interface on either side. In these layers the longitudinal velocity component is $w \approx w_{\mathrm{int}}(x)$, whereas the transverse one due to the continuity equation is given by

$$v \approx -\frac{\mathrm{d}w_{\mathrm{int}}}{\mathrm{d}x}y. \tag{26}$$

Accordingly, the diffusion equation in both fluids reads

$$w_{\mathrm{int}}(x)\frac{\partial c^{(i)}}{\partial x} - \frac{\mathrm{d}w_{\mathrm{int}}}{\mathrm{d}x}y\frac{\partial c^{(i)}}{\partial y} = D_i\frac{\partial^2 c^{(i)}}{\partial y^2}, \tag{27}$$

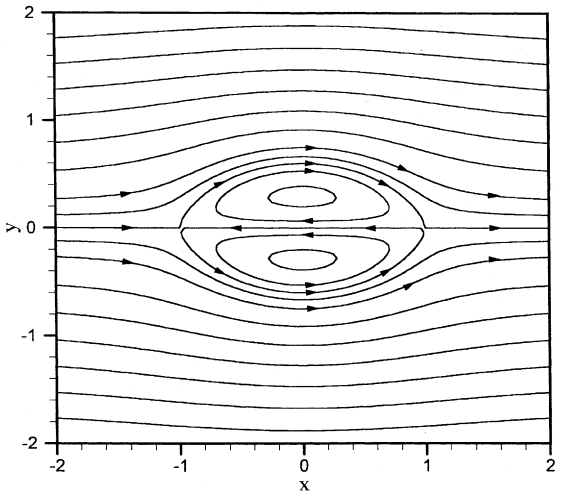

Fig. 14. The calculated flow field (kinematic model 1).

where $c^{(i)}$ $(i = 1, 2)$ is the scalar concentration in layers 1 and 2, respectively, and D_i are the corresponding diffusion coefficients.

Eq. (27) is solved subject to the following boundary conditions:

$$y = -\infty, \quad c^{(1)} = c_\infty^{(1)}, \tag{28}$$

$$y = +\infty, \quad c^{(2)} = c_\infty^{(2)}, \tag{29}$$

$$y = 0, \quad c^{(1)} = c^{(2)}, \tag{30}$$

$$y = 0, \quad -D_1 \frac{\partial c^{(1)}}{\partial y} = -D_2 \frac{\partial c^{(2)}}{\partial y}, \tag{31}$$

where $c_\infty^{(1)}$ and $c_\infty^{(2)}$ are the respective scalar concentrations far from the interface, and the concentration profile and mass flux are continuous at the interface. In this manner Eq. (27) readily yields an analytical solution (cf. [13]) which permits calculation of the mass flux through the interface $j|_{y=0}$, as well as of the mass transfer coefficient

$$h = \frac{j\Big|_{y=0}}{c_\infty^{(1)} - c_\infty^{(2)}}. \tag{32}$$

The corresponding Sherwood number $Sh = ha/D_1$ is given by

$$Sh(x) = \frac{\kappa}{1+\kappa}\frac{2}{\sqrt{\pi}} \times \frac{|w_{\mathrm{int}}(x)|}{\left[\int_{-1}^{x} |w_{\mathrm{int}}(\xi)|\,\mathrm{d}\xi\right]^{1/2}} \left(\frac{V_\infty a}{D_1}\right)^{1/2}, \quad -1 \leqslant x \leqslant 1, \tag{33}$$

where

$$\kappa = \left(\frac{D_2}{D_1}\right)^{1/2} \tag{34}$$

The Sherwood number (33) was calculated under the assumption that the concentrations $c_\infty^{(1)}$ and $c_\infty^{(2)}$ are constant. For qualitative comparison of the results of the numerical calculations of Sections 2 and 3 with those of Eq. (33), the former should correspond to $t << T_\mathrm{d}$, where the diffusion time $T_\mathrm{d} = d^2/D_1$, and $Sc \gg 1$. The result of (33) shows that the mass transfer rate increases as $Pe_\infty^{1/2} = (V_\infty a/D_1)^{1/2}$ which is characteristic of mass transfer enhancement in various vortical flows [7–13].

The calculated distribution of the Sherwood number normalized by $[\kappa/(1+\kappa)](2/\sqrt{\pi})(V_\infty a/D_1)^{1/2}$ is shown in Fig. 15. It is seen that the Sherwood number increases steeply in the vortex near its tip $x = -1$, and then gradually decreases towards the tail of the vortex $x = 1$. This result differs significantly from those described in the preceding section (see Fig. 6), where the local Sherwood number increases near the opposite (with respect to the axial throughflow) tip of the vortex. The difference will be discussed in detail below.

Since the velocity field of the kinematic model 1 is unbounded, we begin with the effect of the wall constraint on the interfacial mass transfer. To elucidate this effect, as well as that of the multiplicity of vortex pairs, we employ another simplified kinematic model. For example, the one of [23] is applicable after appropriate modification to our two-layer case. In [23], a flow mimicking Taylor vortices in a gap filled by a single fluid was considered. The dimensionless stream function was introduced as

$$\psi = \left(y^2 - \frac{1}{4}\right)^2 \sin(\pi x), \tag{35}$$

where y being the radial coordinate across the gap, and x the longitudinal one in it. The gap is assumed to

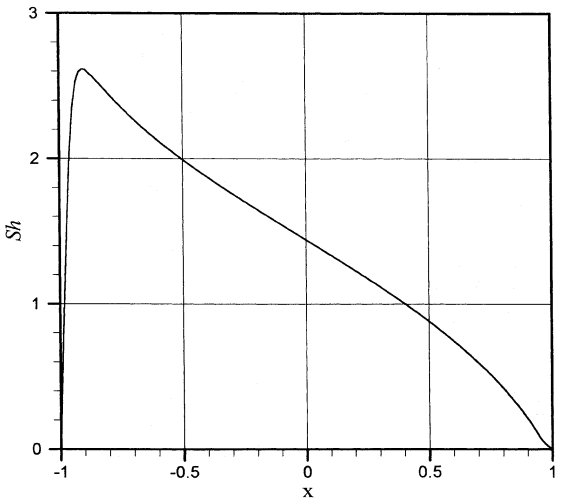

Fig. 15. Normalized distribution of the local Sherwood number in the vortex (kinematic model 1).

extend over $-1/2 \leqslant y \leqslant 1/2$ and $-\infty \leqslant x \leqslant \infty$. The fact that $y = 0$ corresponds to the gap axis means that coordinate is reckoned from the middle of the gap. The stream function (35) generates a system of vortices similar to those of a single layer (the left or the right one in Fig. 2(a)).

For a flow field mimicking the present two-layer system as a whole, we take the following stream function (kinematic model 2)

$$\psi = \left(y^2 - \frac{1}{4}\right)^2 y \sin(2\pi x), \tag{36}$$

which we consider, say, over $0 \leqslant x \leqslant 1$. We assume that the gap is narrow and the curvature effects are negligible. The continuity equation can then be reduced to that for the planar case, which implies

$$w = \frac{\partial \psi}{\partial y}, \quad u = -\frac{\partial \psi}{\partial x}, \tag{37}$$

where w and u are the axial and radial velocity components. Substituting (36) in (37), we obtain

$$w = \left[4y^2\left(y^2 - \frac{1}{4}\right) + \left(y^2 - \frac{1}{4}\right)^2\right] \sin(2\pi x), \tag{38}$$

$$u = -2\pi\left(y^2 - \frac{1}{4}\right)^2 y \cos(2\pi x). \tag{39}$$

It is seen that the no-slip conditions at $y = \pm 1/2$ are satisfied, as well as $u = 0$ at the interface $y = 0$. This means that the kinematic model (36) and (38) and (39) generates a flow field similar to the two-layer flow of Fig. 2(a) (without axial flow). Also from (38) and (39) we find

$$w_{\text{int}} = w|_{y=0} = \frac{1}{16} \sin(2\pi x). \tag{40}$$

Repeating the calculation scheme which led from (27)–(33), we obtain in the present case

$$Sh(x) = C_1 \frac{|w_{\text{int}}(x)|}{\left[\int_0^x |w_{\text{int}}(\xi)|\, \mathrm{d}\xi\right]^{1/2}}, \tag{41}$$

where C_1 is a constant including, in particular, the factor $Pe_\infty^{1/2}$.

Substituting (40) in (41), we find that

$$Sh(x) = C_2 \frac{\sin(2\pi x)}{[1 - \cos(2\pi x)]^{1/2}}, \quad 0 \leqslant x \leqslant \frac{1}{2}, \tag{42}$$

where the constant C_2 also incorporates the factor $Pe_\infty^{1/2}$. Note that as $x \to 0$, the Sherwood number $Sh \to C_2\sqrt{2}$.

The distribution of the Sherwood number (42) resembles that obtained numerically for a similar case in Fig. 2(a). Expression (42) exhibits the same qualitative features: the maximal value of the Sherwood number, $C_2\sqrt{2}$, is achieved at the end of the vortex cell, $x = 0$, and the minimum, 0, in its midpoint at $x = 1/2$. This is also qualitatively similar to the results of numerical calculations presented in Fig. 9(a), as the comparison in Fig. 16 demonstrates. We also show the local Sherwood number calculated from the numerically found interfacial velocity profile and Eq. (41).

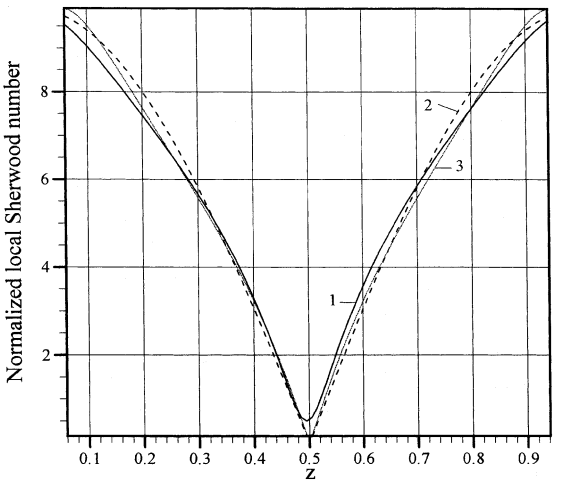

Fig. 16. Normalized local Sherwood number for kinematic model 2 and numerical case (i). 1 – completely numerical, $Pe = 10{,}000$; 2 – kinematic model 2, using Eq. (42) – shifted horizontally; x replaced by z; 3 – semi-analytic, using Eq. (41) and the numerical interfacial velocity profile w_{int}.

To account for the axial flow, we associate the x-axis with the vortices moving with a dimensionless velocity $-W_{\text{drift}} = -(3U/4 - 1/16) < 0$, where U is a constant larger than 1/12. Then instead of (36) we pose (kinematic model 3)

$$\psi = -\frac{1}{16}y + Uy^3 + \left(y^2 - \frac{1}{4}\right)^2 y \cos(2\pi x), \quad 0 \leqslant x \leqslant 1, \tag{43}$$

which mimics the situation shown in Fig. 2(b). From the stream function (43) we find

$$w = -\frac{1}{16} + 3Uy^2 + \left[4y^2\left(y^2 - \frac{1}{4}\right) + \left(y^2 - \frac{1}{4}\right)^2\right] \cos(2\pi x), \tag{44}$$

$$u = -2\pi\left(y^2 - \frac{1}{4}\right)^2 y \sin(2\pi x). \tag{45}$$

Note that in the moving frame the walls move with velocity $3U/4 - 1/16 > 0$. Also, at the interface $y = 0$ the radial velocity component $u = 0$. The axial velocity at the interface according to (44) and (45) is given by

$$w_{\text{int}}(x) = \frac{1}{16}[\cos(2\pi x) - 1]. \tag{46}$$

Using (41) and (46), we obtain

$$Sh(x) = C_3 \frac{[1 - \cos(2\pi x)]}{[x - \sin(2\pi x)/2\pi]^{1/2}}, \quad 0 \leqslant x \leqslant 1, \tag{47}$$

where the constant C_3 incorporates the factor $Pe_\infty^{1/2}$. As $x \to 0$, the Sherwood number $Sh \to 0$.

The distribution (47) is shown in Fig. 17 with the constant C_3 adjusted so that the maximum of (47) coincides with that of the numerically calculated $Sh(x)$. It is clearly seen that both kinematic models 1 and 3 predict the maximum of the local Sherwood number close to the front stagnation point, and the numerical result – the one close to its rear counterpart. Therefore, allowance for the wall constraint in the kinematic model, as well as for multiplicity of vortices cannot eliminate the disagreement between model 1 and the numerical results. Further, we substituted the numerically obtained interfacial velocity profile in Eq. (41), and the result, also shown in Fig. 17, again qualitatively disagrees with the numerically obtained $Sh(x)$. At the same time, substitution of the velocity defined by Eqs. (44) and (45) into the completely numerical model (9)–(14) yields a dependence $Sh(x)$ similar to the completely numerical result.

Analysis of the discrepancy revealed the following. All numerical results were obtained with Reynolds number $Re = O(10^3)$ and Peclet number $10^3 \leqslant Pe \leqslant 10^4$, which means that the corresponding Schmidt number is $Sc = Pe/Re = 1$ to 10. (Note that calculations with $Pe > 10^4$ necessitate a very fine grid near the interface and, as a result, prohibitive time consumption). In such situations the thin diffusional boundary layer does not develop, since $Sc \gg 1$ is not reached. As a result, the mass transfer in the numerical calculations occurs over the whole vortex cell in the y-direction, instead of in the thin diffusional boundary layer alone (at intermediate times). Then the concentration distribution far from the interface is not independently fixed and uniform, as implied by the boundary conditions (28) and (29), but is directly affected by the interfacial mass transfer and vice versa. On the other hand, the analytical solution for the concentration (cf. [12,13]) against the background of the expressions (41), (42) and (47) for the Sherwood number, concerns the extremely thin boundary layers (corresponding to $Sc = O(10^3)$ which is a realistic value for proteins). Such cases correspond to $Pe \geqslant 10^6$, and are not amenable to the numerical technique used in the present study. Note also that the better agreement between the analytical and numerical approach obtained for the case without throughflow (Fig. 16) refers to the already obtained boundary layer scaling $Sh \sim Pe^{1/2}$, while in the presence of throughflow this scaling was not reached numerically (cf. Fig. 10(a) and (b)).

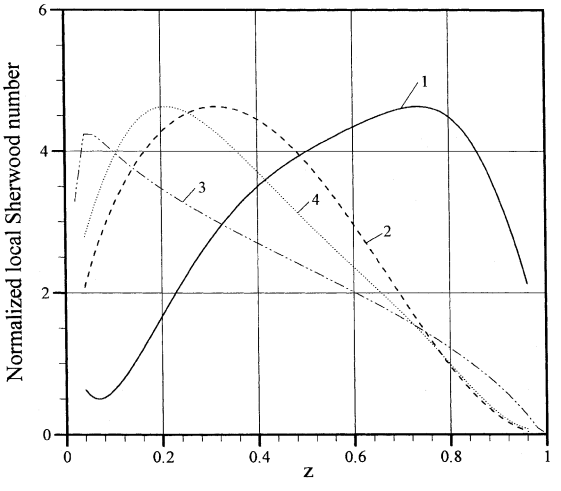

Fig. 17. Normalized local Sherwood number for kinematic model 3 and numerical case (iii). 1 – completely numerical, $Pe = 10{,}000$; 2 – kinematic model 3, using Eq. (47) – shifted; x replaced by z; 3 – kinematic model 1, using Eq. (33) – shifted; x replaced by z; 4 – semi-analytic, using Eq. (41) and the numerical interfacial velocity profile w_{int}.

It is emphasized that the origin of the discrepancy lies not in the quality of the kinematic models (which mimic the real velocity field quite reasonably) but in the fact that the numerically solved refers to the case of $Sc = 1$ to 10, and the analytical one to $Sc \gg 1$.

It is also emphasized that in any case it is impossible, within the framework of any kinematic model, to investigate the Reynolds number dependence (for the axial flow) of the advection–diffusion effects.

5. Concluding remarks

Two-fluid Taylor–Couette flow develops pairs of vortical cells. Such a flow is a key element of a novel extractor described in [1,2]. In this case a passive scalar (a protein) is initially present in one fluid layer, and is to be transferred into another. Since the diffusion coefficients of proteins are extremely small (the corresponding Schmidt number is $Sc = O(10^3)$), purely diffusional interfacial mass transfer is ineffective. In the present work it is shown that the vortex cells result in steeper concentration gradients near the interface, which leads to increase of the Sherwood number Sh with $Pe^{1/2}$ (Pe being the Peclet number).

It is also shown that axial flow imposed on the two-layer Taylor–Couette vortex system has a strong effect on both the flow pattern and the mass transfer through the liquid–liquid interface. As a result, the distribution of the local Sherwood number becomes asymmetric and the average mass transfer coefficient (average Sherwood number) decreases. At the Schmidt number $Sc = 1$ to 10 maximal local mass transfer is observed at the tip of the Taylor vortex where the fluid flow is directed towards the interface. The effect takes place due to convective mass transport by the Taylor vortices.

In spite of the fact that the scaling $Sh \sim Pe^{1/2}$ is demonstrated for both $Sc = 1$ to 10 and $Sc \gg 1$

(numerically, only without throughflow), the distribution of the Sherwood number along the interface differs qualitatively in these two cases. The difference is related to the fact that in the first case the mass transfer occurs over the whole vortical cell, not only in an extremely thin diffusional boundary layer near the interface as in the second case.

Acknowledgements

This research was supported by BSF (US–Israel Binational Science Foundation) grant No 97-118.

References

[1] G. Baier, M.D. Graham, E.N. Lightfoot, Mass transport in a novel two-fluid vortex extractor, AIChE J. 46 (2000) 2395–2407.
[2] G. Baier, M.D. Graham, Two-fluid Taylor–Couette flow: experiments and linear theory for immiscible liquids between corotating cylinders, Phys. Fluids 10 (1998) 3045–3055.
[3] G. Baier, T.M. Grateful, M.D. Graham, E.N. Lightfoot, Prediction of mass transfer rates in spatially periodic flows, Chem. Eng. Sci. 54 (1999) 343–355.
[4] T. Howes, M. Rudman, Flow and axial dispertion simulation for travelling axisymmetric Taylor vortices, AIChE J. 44 (1998) 255–262.
[5] G.K. Batchelor, On steady laminar flow with closed streamlines at large Reynolds number, J. Fluid Mech. 1 (1956) 177–190.
[6] P.B. Rhines, W.R. Young, How rapidly is a passive scalar mixed within closed streamlines?, J. Fluid Mech. 133 (1983) 133–145.
[7] E. Guyon, Y. Pomeau, J.P. Hulin, C. Baudet, Dispersion in the presence of recirculating zones, Nucl. Phys. B (Proc. Suppl.) 2 (1987) 271–280.
[8] B.I. Shraiman, Diffusive transport in a Rayleigh–Benard convection cell, Phys. Rev. A 36 (1987) 261–267.
[9] M. Piva, A. Calvo, A. Aguirre, G. Callegari, S. Gabbanelli, M. Rosen, J.E. Wesfreid, Hydrodynamical dispersion in Taylor–Couette cells, J. Phys. III France 7 (1997) 895–908.
[10] M.N. Rosenbluth, H.L. Berk, I. Doxas, W. Horton, Effective diffusion in laminar convective flows, Phys. Fluids 30 (1987) 2636–2647.
[11] E.L. Vold, Computational simulations of vorticity enhanced diffusion, Phys. Fluids 11 (1999) 3353–3668.
[12] A.L. Yarin, G. Brenn, O. Kastner, D. Rensink, C. Tropea, Evaporation of acoustically levitated droplets, J. Fluid Mech. 399 (1999) 151–204.
[13] A.L. Yarin, Stationary dc streaming due to shape oscillations of a droplets and its effect on mass transfer in liquid–liquid interfaces, J. Fluid Mech. (in press).
[14] A.L. Yarin, T.A. Kowalewski, W.J. Hiller, St. Koch, Distribution of particles suspended in 3-D laminar convection flow, Phys. Fluids 8 (1996) 1130–1140.
[15] A.Yu. Gelfgat, P.Z. Bar-Yoseph, A. Solan, Stability of confined swirling flow with and without vortex breakdown, J. Fluid Mech. 311 (1996) 1–36.
[16] A.Y. Gelfgat, P.Z. Bar-Yoseph, A. Solan, Vortex breakdown and instability of swirling flow in a cylinder with rotating top and bottom, Phys. Fluids 8 (1996) 2614–2625.
[17] C.S. Peskin, Numerical analysis of blood flow in the heart, J. Comput. Phys. 97 (1977) 220–252.
[18] W. Schröder, H.B. Keller, Wavy Taylor-vortex flows via multigrid-continuation methods, J. Comput. Phys. 91 (1990) 197–227.
[19] C.D. Andereck, S.S. Liu, H.L. Swinney, Flow regimes in a circular Couette system with independently rotating cylinders, J. Fluid Mech. 164 (1986) 155–183.
[20] B.S. Ng, E.R. Turner, On the linear stability of spiral flow between rotating cylinders, Proc. Roy. Soc. London A 382 (1982) 83–102.
[21] G. Baier, M.D. Graham, Two-fluid Taylor–Couette flow with countercurrent axial flow: linear theory for immiscible liquids between corotating cylinders, Phys. Fluids 12 (2000) 294–303.
[22] A.B. Shabat, On one scheme of flow of ideal fluid in the case of a trench on the bottom, J. Appl. Mech. Tech. Phys. 68 (4) (1962) (in Russian).
[23] D.S. Broomhead, S.C. Ryrie, Particle paths in wavy vortices, Nonlinearity 1 (1988) 409–434.